Wear 552-553 (2024) 205460

Contents lists available at ScienceDirect

Wear

journal homepage: www.elsevier.com/locate/wear

Wear study of additively manufactured repair material for R260 grade rails

B. Rodríguez-Arana [a,b,*], J. López-López [a,b], F. Schiopetto [a,b], A. San Emeterio [a,b], F. Salas Vicente [c], I. Pérez-Casero [a,b], A. Veiga [a,b], S. Ausejo [a,b]

[a] Ceit-Basque Research and Technology Alliance (BRTA), Manuel Lardizabal 15, 20018, Donostia / San Sebastián, Spain
[b] Universidad de Navarra, Tecnun, Manuel Lardizabal 13, 20018, Donostia / San Sebastián, Spain
[c] Mechanical and Materials Engineering Department, Universitat Politècnica de València, Camino de Vera S/n, 46022, Valencia, Spain

ARTICLE INFO

Keywords:
Wheel-rail contact
Wear test
Twin-disc
Additive manufacturing
Rail maintenance

ABSTRACT

Additive Manufacturing (AM) has been considered as a promising method for repairing rails and extending their service life. In this work, the wear rates of twin-disc specimens produced through laser additive manufacturing against ER7 material are studied applying creepages from 0.4 % to 2.6 %. The approved E11018-G electrode material is atomised and fully cladded into twin-disc rail specimens by Laser Powder Directed Energy Deposition. After the weight loss tests at 1400 MPa, experimental results are fitted with the theoretical adhesion curve modifying FASTSIM coefficients. This adhesion curve is employed to numerically calculate the slip contact area of each test. A non-linear correlation has been found and defined between wear and the slip area including the non-linear zone. This relationship is identified for tribochemical wear for low creepages and delaminative wear for middle and high creepages by surface and metallographic characterisation. The obtained results allow to predict the wear of the additively manufactured E11018-G repair material under wheel-rail contact conditions when the slip area is known.

1. Introduction

Railway tracks are subjected to different degradation mechanisms like rolling contact fatigue (RCF) and wear on rails due to vehicle-track interaction. The apparition of defects, that could potentially represent a safety hazard, requires maintenance tasks with a great impact on the Life Cycle Cost. To extend the lifespan of rails and prevent the rail replacement, localized repairs of defects are typically performed by traditional welding techniques. Currently, Shielded Metal Arc Welding (SMAW) stands as the most used technology for repairing rail defects [1,2]. Although the weldability of rails with approved materials has been investigated [3], no studies are found in characterising the wear of the repairs.

For the last decade, the use of Laser Powder Directed Energy Deposition (LP-DED) has been studied as an alternative for rail restoration due to its benefits, including its low substrate heat affection and the eliminations of human error in repairs via process automation [4]. Lewis et al. [5–7], investigated the wear rate of several powders deposited using LP-DED on R260 and R200 rail grades. Their findings demonstrated that special alloys such as Stellite 12 and MSS alloys provided superior wear resistance compared to the parent R260 and R200, demonstrating the feasibility of LP-DED technology. Although there are many studies evaluating the wear of laser cladding on railway rails and wheels [8–11] to the best of the authors' knowledge, no other research exists on determining wear rates of approved electrodes or materials for rail repair, such as the E11018-G. This research gap is significant given its pivotal role in comprehending the potential longevity of a rail repair. The wear rate study of approved materials manufactured by LP-DED will allow the progress, in the development and implementation, of this technology in the railway sector.

In wheel-rail contact, wear is not only related to the normal load between rolling solids but also to the shear stress at the contact and the slip. Creepages, the kinematical deviation from the pure rolling motion, are null at full-stick contact and no wear occurs. In railway dynamics, very low creepages are observed, approximately 1 % in sharp curves. According to the literature, creepages are considered low up to 2–3% [12,13]. Two types of models are used in the literature for the assessment of wear [14]. On the one hand, sliding models, in which the volume of wear is proportional to the sliding distance and normal force and inversely proportional to the material hardness. This is known as Archard's wear model [15,16] which can be recalibrated to predict wheel and rail profile change [17,18]. On the other hand, energy

* Corresponding author. Parque Tecnológico de San Sebastián - Paseo Mikeletegi, Nº 48, 20009, Donostia - San Sebastián, Spain.
E-mail address: brodriguez@ceit.es (B. Rodríguez-Arana).

https://doi.org/10.1016/j.wear.2024.205460
Received 26 March 2024; Received in revised form 23 May 2024; Accepted 18 June 2024
Available online 19 June 2024

transfer models assume wear loss as a function of the energy dissipation in the contact patch [19,20]. According to Al-Maliki et al. [21], wear rates can be also defined by some parameters of the material, the maximum traction pressure, and the depth of the damaged layer. To calculate the contact patch considering a three-dimensional problem FASTSIM, the numerical implementation of Kalker's simplified theory [22], is widely used for dynamic simulations. Once the contact patches and the wear volume are known, worn wheel or rail profiles can be calculated by numerical techniques [23,24].

The main objective of this work has been to study the wear rates of LP-DED specimens made using powder grade E11018-G electrode material against discs of ER7 material. First, weight loss measurements as a function of creepage on twin-disc set-up and the adhesion curve on a scaled test bench are obtained. After twin-disc cycles wear mechanism is investigated by surface and metallographic characterisation. Then, a tribological model is developed considering wear rates at full slip conditions from the weight loss raw values using a modified FASTSIM algorithm. Next, a discussion of the results is presented. Finally, the last section presents the most relevant conclusions of this paper.

2. Experimental procedures

The experimental procedures consist of three different parts: preparation of materials and specimens, twin-disc tests for 8 pairs of discs to obtain weight loss measurements and an additional test on a scaled test bench with larger specimens to obtain the adhesion curve of the LP-DED cladded material.

2.1. Material and specimens

The twin-disc wheel specimens were cut from an ER7 wheel, while rail specimens were obtained from LP-DED cladded C45 bars using powder grade E11018-G electrode as filler material. From now on, twin-disc wheel and rail specimen will be known as ER7 and LP-DED specimens respectively. The scaled test bench rail specimen was obtained by cladding same powder material into a C45 scale bench disc. Fig. 1 shows the manufactured twin-disc and scaled test bench LP-DED specimens before machining while Fig. 2 shows a schematic diagram of both rail discs after machining for testing.

The chemical composition of ER7 and LP-DED specimens and the rail base material (C45) is shown in Table 1. The chosen E11018-G electrode is a special material for repairing R260 grade rails commercially known as OK75.75 [25]. The resurfacing of rails is normally done by SMAW following the guidelines of the American Welding Society on isolated

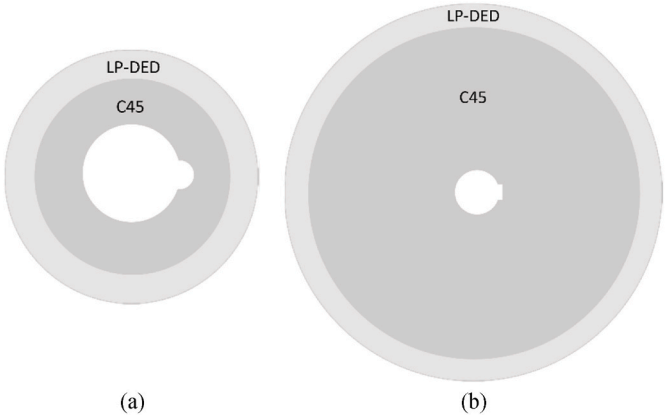

Fig. 2. Schematic diagram of LP-DED specimens after machining for (a) fully cladded twin-disc and (b) fully cladded scaled test bench.

Table 1
Chemical composition of the specimens and rail base material (%wt).

	C	Si	Mn	P	S
Wheel (ER7)	0.52	0.31	0.79	0.010	0.002
Rail (LP-DED)	0.05	0.36	1.60	–	–
Rail base material (C45)	0.45	0.40	0.70	0.045	0.045

defects such as wheel burn, squats, shelling, or superficial head checks [26]. Experimental atomisations of the E11018-G material were performed at CEIT facilities in a small-scale research atomisation unit (*PSI model HERMIGA 75/3VI*). Rail specimens were prepared using a custom-made LP-DED cell at CEIT. The powder was deposited on the C45 bar and scaled test bench disc using a 4-kW laser (*IPG Photonics*) with a wavelength of 1070 nm. The powder flow rate was supplied by an *Oerlikon Twin 150* powder feeder using argon as carrier and shielding gas. The LP-DED head was a *Kuka MWO-I Powder* with motorized optics (adjustable laser spot size from 1.0 to 4.8 mm) and a 3-jet nozzle. A 6-degree-of-freedom *Kuka* robot was used to move the LP-DED head. The bar and the scaled test bench disc were fixed to a positioner with 2 degrees of freedom.

As shown in Fig. 3, the ER7 wheel material has a ferrite-pearlite microstructure while LP-DED rail material has a pure ferritic microstructure.

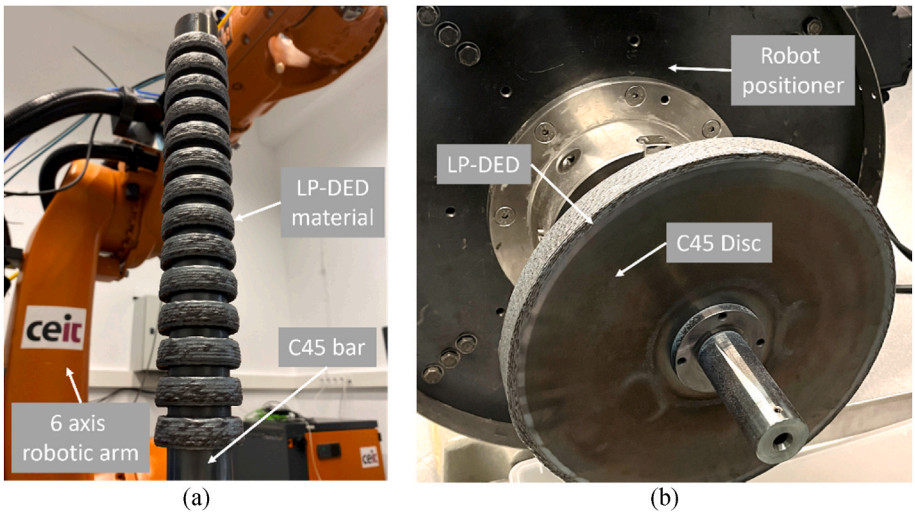

Fig. 1. Manufactured LP-DED specimens before machining for (a) fully cladded twin-discs and (b) fully cladded scaled test bench.

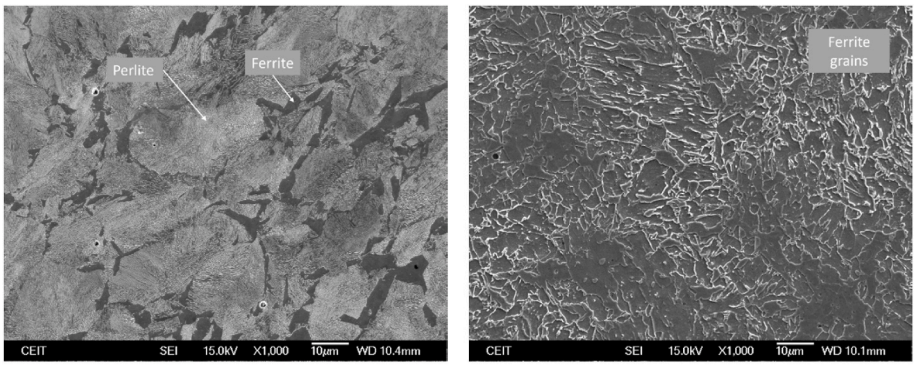

(a) (b)

Fig. 3. Microstructures of tested materials. (a) Wheel (ER7). (b) Rail (LP-DED).

2.2. Weight loss measurements

Wear testing was performed on the UPV (Universitat Politècnica de Valencia) twin-disc tester whose design is based on "SUROS" machine [27] of The University of Sheffield. It is based on two electric drives that transmit a direct rotary motion to both discs. A pneumatic actuator, connected to a load cell, applies a normal load between the two discs. A torque transducer measures the side of the rail specimen. Consequently, the tangential force between discs is calculated with the known radius of the rail specimen. The relationship between the tangential force and the normal force, acquired from the load cell, provides the traction coefficient at each time step. A schematic representation of the machine can be seen in Fig. 4.

Flat surfaces in the lateral direction are recommended for twin-disc wear damage tests, even though real wheel and rail profile have crowned surfaces [28]. In this way, the contact area remains practically constant with the wear of the disc surfaces, avoiding changes in contact pressure for the same normal load. Fig. 5 shows the assembly of discs, where the LP-DED rail specimen is 8 mm wide and the ER7 wheel specimen is 15 mm wide. Differences in width ensure proper contact between the samples during the experiment, and a constant contact width of 8 mm can be considered. To obtain robust and reliable results, it is essential to properly define the twin-disc test set-up. In the present study, the LP-DED and ER7 specimens act as the driven and the driving discs, respectively. The creepages are reached by accelerating the driving disc to simulate an acceleration situation.

Table 2 contains the parameters of different tests, in which normal pressure and linear speed remain constant. The table includes the radio of each specimen (R1 and R2), the applied normal load W to achieve the desired maximum normal pressure Po, and the corresponding average value Pavg. Additionally, the contact area A between the specimens for each test is provided.

As an example of a twin-disc test, Fig. 6 shows the traction coefficient during the four stages tested at 2.00 % of creepage. These steps are for 10, 30, 50 and 70 kilocycles. Before testing and after each step, both discs were cleaned by brushing with ethanol, dried and weighed using a balance with an accuracy of 0.1 mg. At the beginning of each stage, some cycles (for this case, the first 7000 cycles) are necessary to reach a stable value. The first running-in stage, in which the change in the traction coefficient is more evident, is just of 10 kilocycles. At this stage, it is necessary to remove the outer layer and promote the surface and subsurface changes that will accompany both discs through the rest of the test (such as hardening, subsurface deformation, surface oxidation and crack initiation). Although generally three stages are performed to reach 50 kilocycles, two tests were performed up to 70 kilocycles to confirm the wear trend.

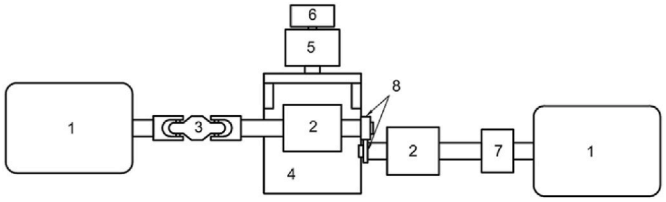

Fig. 4. Scheme of the twin-disc test machine. 1: Servomotors; 2: Bearings; 3: Double cardan joint; 4: Sliding table; 5: Hydraulic cylinder; 6: Load cell; 7: Torque and rotational speed transducer; 8: Test discs.

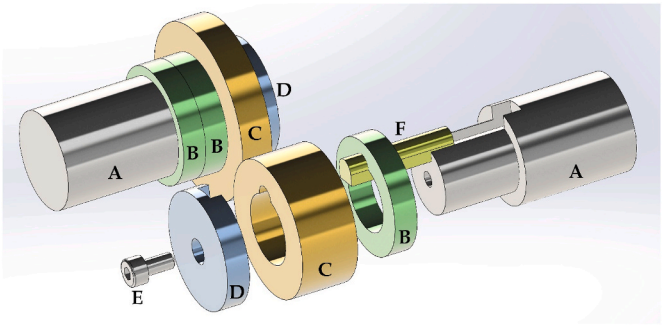

Fig. 5. Discs assembly. A: Shafts, B: positioning discs, C: test discs, D: washer discs, E: bolts, and F: shaft key.

The weight loss (*WL*) of LP-DED and ER7 specimens is shown in Fig. 7. Generally, the slope increases with both the creepage value and the number of cycles. The *WL* obtained for ER7 material is lower than the obtained with LP-DED material. Note that for ER7 at 2.6 % creepage, there is an offset for one of the pairs (used previously in another test) due to the first stage of 10 kilocycles and then the slopes are similar for the same creepage value.

From *WL* values, the wear rate *K* is calculated as

$$K = \frac{WL}{d \bullet A} \,. \tag{1}$$

where *A* is the total area of the contact patch and *d* is the travelled distance according to the number of cycles and the perimeter of specimens. Fig. 8 shows *K* values against the wear index (defined as $T\gamma/A$) of both materials. For this assessment, the *WL* values for 10 kilocycles are excluded and the *WL* between stages of 20 kilocycles are considered. The feature of this comparison is that, in laboratory tests, different loads, friction coefficients and bodies shape configuration could provide the same wear rate for the same $T\gamma/A$ values. Nevertheless, as proposed by Butini et al. [29] laboratory test results should be scaled to be applied to real scenarios using an experimental law [30]. In the present work, LP-DED specimens show a higher wear rate than the ER7 material.

Table 2
Parameters of each tested condition.

Creepage	0.4 %	0.4 %	1.5 %	1.5 %	2.0 %	2.0 %	2.6 %	2.6 %
Test	1	2	3	4	5	6	7	8
R1 LP-DED (mm)	22.12	22.12	22.12	21.12	21.12	21.12	22.12	22.12
R2 ER7 (mm)	17.5	17.5	17.5	16.5	16.5	16.5	17.5	17.5
W (kN)	4.14	4.14	4.14	3.93	3.93	3.93	4.14	4.14
A (mm^2)	3.76	3.76	3.76	3.57	3.57	3.57	3.76	3.76
Pavg (GPa)	1.10	1.10	1.10	1.10	1.10	1.10	1.10	1.10
Po (GPa)	1.40	1.40	1.40	1.40	1.40	1.40	1.40	1.40

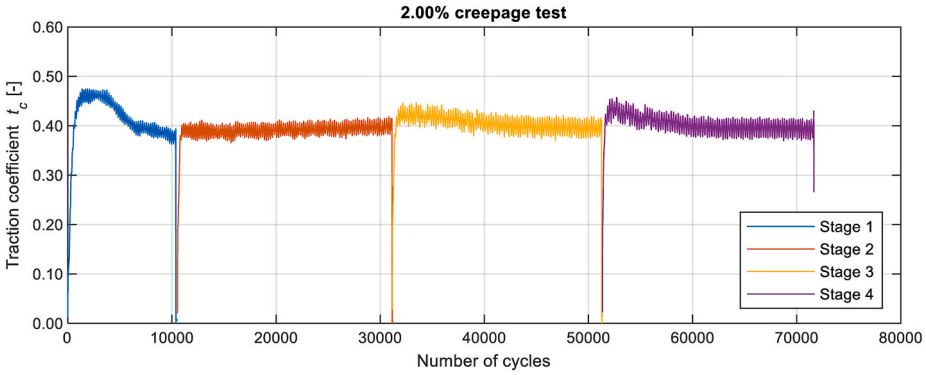

Fig. 6. The whole traction coefficient for all stages of the 2.00 % longitudinal creepage test.

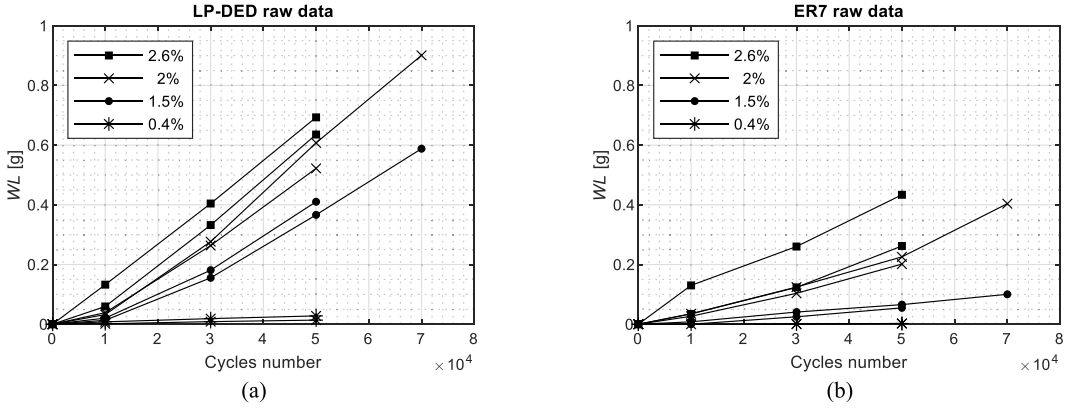

Fig. 7. Weight loss obtained from twin-disc at tested creepages for (a) LP-DED and (b) ER7 materials.

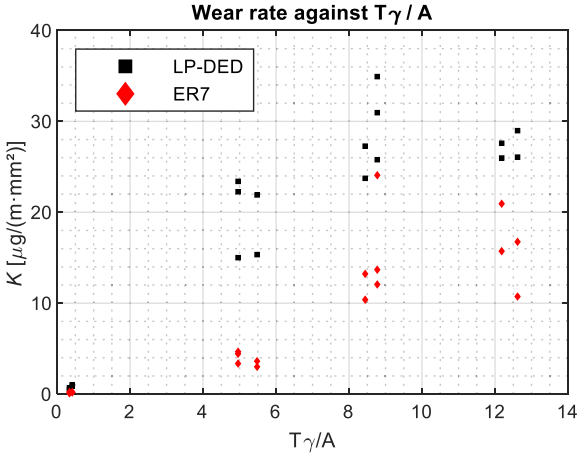

Fig. 8. Wear rates against the average Tγ/A of tested creepages.

Moreover, the wear rates of LP-DED specimens are around 4 times higher than the values shown in the literature for R260 grade rails [31]. Compared with other clad materials this electrode material should be classified in the third group according to Lewis et al. [32]. Wear is influence by the choice of which disc acts as the driving or driven disc, or whether braking or acceleration conditions are being simulated [33]. R. Lewis et al. [34] reported that for the R7/900A pair material, the driving disc wears the most and is the one on which debris adheres during a twin-disc test. Although for conventional materials, specimens acting as driving discs (ER7) may exhibit the highest wear rates, microstructural differences (see Fig. 3) between the two materials could be the cause of this difference, with the driven discs (LP-DED) experiencing the highest wear rates.

2.3. Adhesion curve

The adhesion curve obtained with twin-disc tests differs from a real scenario due to the shape and dimensions of the specimens. Scaled test benches enable experimental characterisation of the wheel-rail contact problem. The scaled test bench designed by Alonso et al. [35] at CEIT

can assess the influence of lateral creepage and spin. The main drawback of these benches is that, due to their size, it is difficult to obtain samples of real wheels and rails. In order to obtain the adhesion curve, in this work, this test bench was used with a scaling dimensional factor of 1/5 (see Fig. 9). Therefore, an equivalent normal load 25 times lower is applied to obtain an elliptical contact path with the same aspect ratio as a real one. In this way, the normal pressure (and surface tractions for a tested creepage) reach the same values as in a real scenario.

The disc used as rail in the scaled test bench (see Fig. 9) was coated by LP-DED (see Fig. 1) and lathed with a curved shape in the transversal direction. Fig. 10 shows the values of the traction coefficient obtained by calculations (using the FASTSIM algorithm [36,37]), by a test performed in 2021 and by the test performed within this research work using the LP-DED material.

The experimental adhesion curve with LP-DED material is equivalent to that expected with a conventional material. Therefore, the tangential forces should be similar if the creepage is the same.

3. Wear damage characterisation

As a means of comparison, twin-disc wear damage characterisation was performed on specimens tested after 50k cycles. The surfaces and internal microstructure characterisation of the LP-DED and ER7 specimens subjected to 0.4 %, 1.5 % and 2.6 % creepages is done as follows.

3.1. Surface analysis

Photographs and SEM micrographs of specimens worn surfaces are shown in Fig. 11 and Fig. 12.

The rail and wheel discs tested at the lower creepage (0.4 %) present a reddish tone (Fig. 11 (a) and (b)), due to an oxidative wear process confirmed by EDS analysis (Fig. 13). This oxidative tribochemical wear process is expected in this creepage regime for conventional wheel and rail materials [38].

Medium creepage condition specimens (1.5 %) exhibit cracks, peeling and spalling wear damage (Fig. 12 (c) and (d)). The surfaces of the specimens tested under 2.6 % of creepage are the most damaged among all. LP-DED specimen exhibits numerous surface cracks, whereas the ER7 specimen shows fewer but larger cracks (Fig. 12 (e) and (f)). In all creepage condition, LP-DED specimens present a more damage surface than their ER7 counterparts.

3.2. Microstructural analysis

Internal microstructural characterisation is performed to evaluate the depth and the extent of damage of twin-disc tested specimens. Cross sections of the specimens were cut in the direction parallel to the rolling movement. Each section was mounted in conductive resin, polished to 1 μm diamond and etched with 2 % nital to be observed under optical and SEM microscopes.

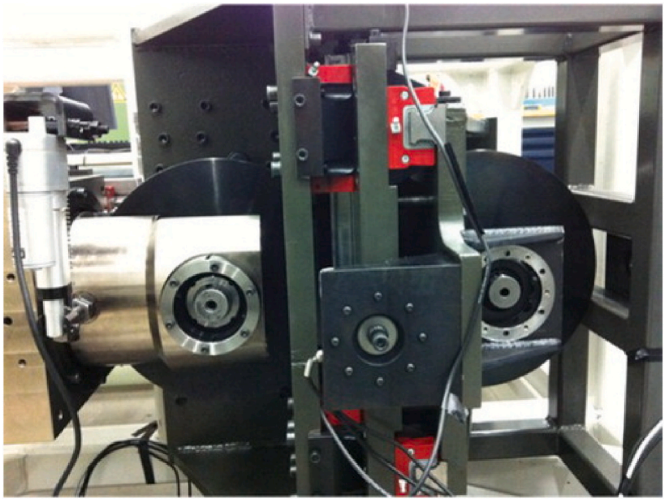

Fig. 9. Scaled test-bench picture at Ceit facilities [35].

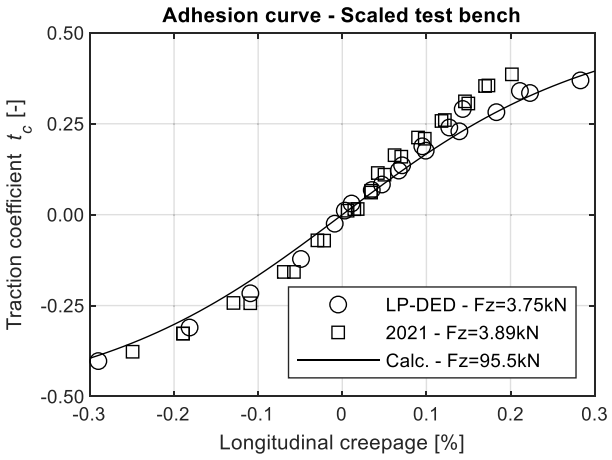

Fig. 10. Adhesion curve test at 250 rpm and a target normal load of 3.6 kN using braking torque.

Fig. 14 shows the optical micrographs of specimens near the contact surface after twin-disc test. For all specimens, the depth of microstructural deformation increases with the tested creepage. The LP-DED specimens show deeper plastic deformation than their ER7 counterparts. The ferritic microstructure of LP-DED specimens shows a higher deformation due to the low yield strength of the ferrite. This observation is consistent with microhardness profiles shown in Fig. 15, which present a deeper hardening for the ferritic structure of the LP-DED specimens. The hardness of specimens before the tests is observable for surface distances greater than 0.7 mm (~275 HV03 for ER7 and ~250 HV03 for LP-DED), where specimens are not affected by the tested creepages. The difference in hardness of specimens influences the obtained wear rates. The plastic deformations and hardness profiles are in accordance with those presented by other authors tested in similar conditions [39–41].

Fig. 16 illustrates the microstructure at higher magnification of the LP-DED disc tested at 1.5 % of creepage. It shows the microstructure evolution from the surface to the inside of the LP-DED specimen. Very close to the surface, a fine ferrite microstructure is observed (see Fig. 16 (b) and (c)). In the middle zone, a tilted and moderately deformed ferrite microstructure is found (see Fig. 16 (d) and (e)). In the innermost zone of the disc, the undeformed ferrite microstructure can be seen (see Fig. 16 (f) and (g)). After twin-disc deformation and grain refinement, a fine ferritic microstructure is generated [42], which will undergo the wear mechanisms. Same microstructural evolution is found in the LP-DED specimen tested at 2.6 % creepage.

Cross-sections corresponding to the twin-disc specimens examined under scanning electron microscopy are shown in Fig. 17. LP-DED and ER7 specimens tested at 0.4 % of creepage show surface oxidation and no cracks (Fig. 17 ((a) and (d)). Internal spherical micro-oxides due to the manufacturing process are only observed in the LP-DED specimen. In contrast, the LP-DED and ER7 specimens tested at 1.5 % and 2.6 % creepage show a higher damage state (Fig. 17 ((b-e) and (c-f)). The observed wear mechanisms are different for ER7 and LP-DED specimens.

The LP-DED specimens show surface parallel cracks, debris and internal micro-oxides (Fig. 17 (b) and (c)). The cracks propagate parallel to the surface through the refined ferrite microstructure (Fig. 18). The fracture of these cracks shown in Fig. 17 (b) and (c) is the cause of the peeling and spalling previously shown in Fig. 12. As can be seen in Fig. 19, the internal micro-oxides act as crack propagation points,

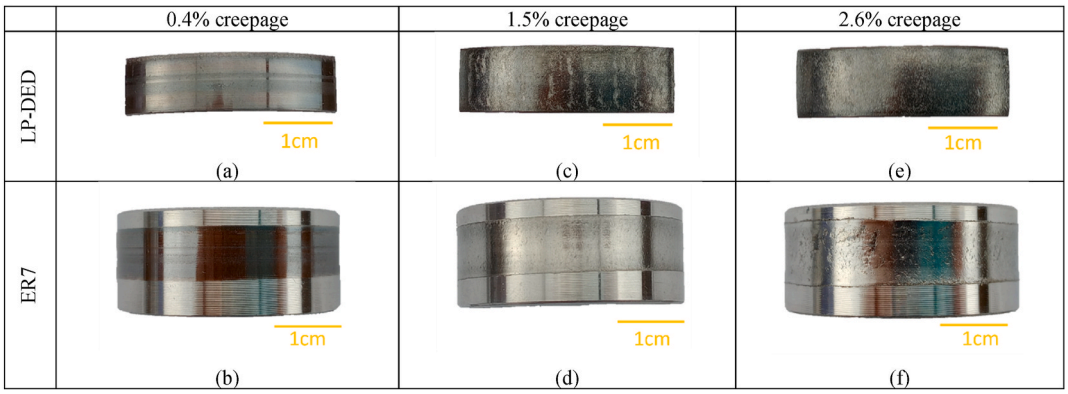

Fig. 11. Photographs of surface appearance of rail and wheel discs at the end of 50000 cycles preformed with different creepages.

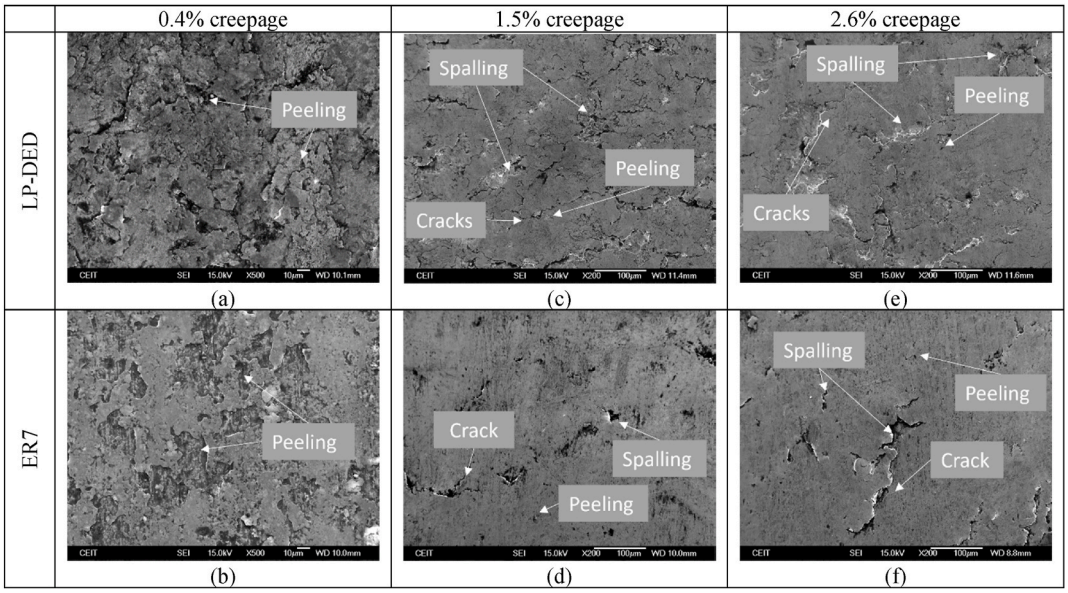

Fig. 12. Superficial SEM micrographs of rail and wheel discs at the end of 50000 cycles performed with different creepages. 500× Initial magnification (0.4 % creepage) and 200× Initial magnification (1.5 % and 2.6 % creepages).

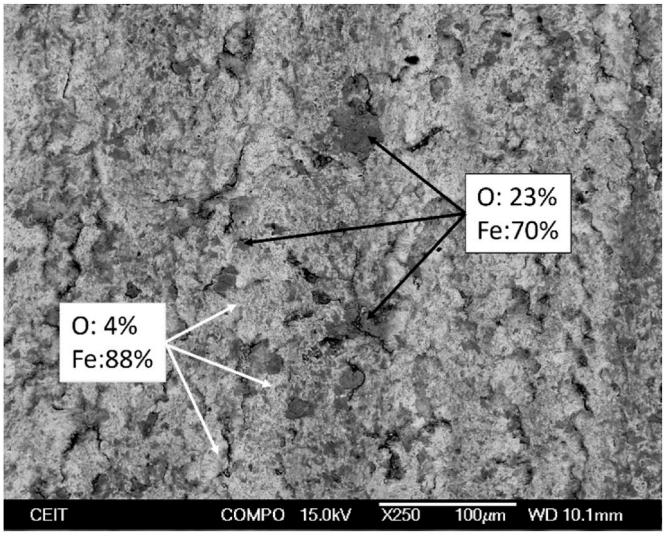

Fig. 13. SEM-EDAX analysis. 0.4 % creepage rail specimen. 250× magnification.

increasing the wear of studied specimens [43]. Fig. 20 (a) shows flakes from LP-DED specimen forming surface debris after compact. As expected, EDS analysis shown in Fig. 20 (b) confirms that debris are highly oxidized [41]. Fig. 21 (a) shows a semi-continuous surface layer of debris, which degrades as twin-disc cycles continue (see Fig. 21 (b)).

In contrast, the ER7 specimens tested at 1.5 % and 2.6 % of creepage only show surface and sub-surface cracks (Fig. 16 (e) and (f)). Fig. 22 shows how cracks propagate into the material and then runs parallel to the surface of the disc. After several cycles, the material above fractures resulting in the material ejection from the wheel surface. When the ferrite-perlite microstructure of the ER7 specimens deforms, the ferrite shapes to soft ferrite lines while the pearlite breaks. Cracks preferentially initiate and develop along the ferrite lines because of their low-stress limit. This wheel wear mechanism is consistent with studies publish by H·H.Ding et al. [39,40].

Summarizing, the following mechanism were found after twin-disc specimen characterisation.

- Oxidative wear in LP-DED and ER7 specimens tested at 0.4 % creepage.
- Deep cracks that after certain penetration run parallel to the disc surface specimens tested at 1.5 % and 2.6 % creepage.

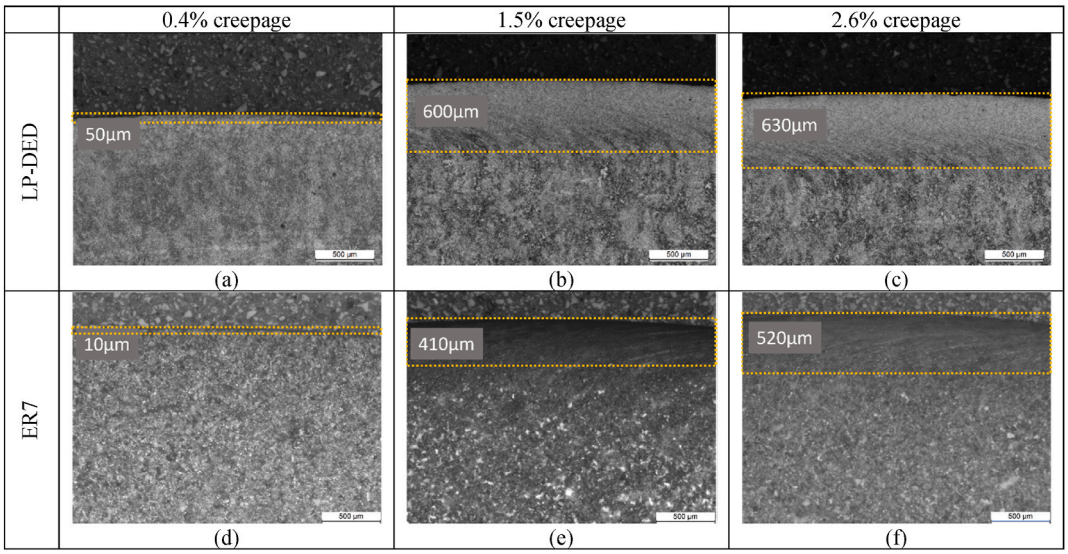

Fig. 14. Optical micrographs of plastic deformation of (a–c) LP-DED and (d–f) ER7 specimens under different creepages.

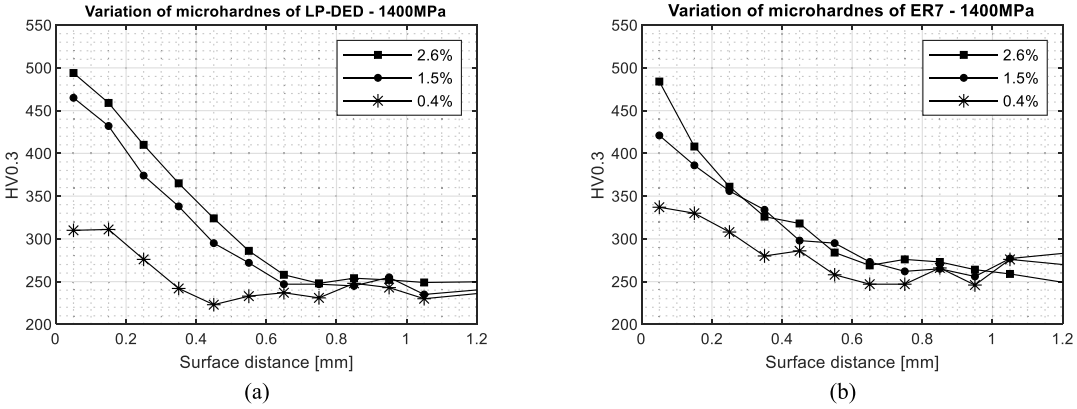

Fig. 15. Variation of microhardness as a function of the distance from the worn surface for (a) LP-DED cladded rail and (b) ER7 wheel.

- Delaminative wear, consisting of cracking, peeling, and spalling with the contribution of debris and internal oxides in LP-DED specimens tested at 1.5 % and 2.6 % creepage.

This is in agreement with the wear rate (K) observed in Fig. 8, in which LP-DED specimens wears more than their ER7 counterparts.

4. Wear rates at full slip

In this section, the wear rates of twin-disc test are assessed for different creepage values, considering the area slipping in the contact patch. For that purpose, as proposed in Ref. [41], the variant of wear rate is employed using the slipping area A_{slip} defined as

$$K_{slip} = \frac{WL}{d \bullet A_{slip}} . \tag{2}$$

The contact conditions from the different creepages values tested, such as the total contact path area A and the A_{slip}/A ratio, can be obtained solving the tangential contact problem. The analytical adhesion curve can be obtained from tests performed by modifying the c_{11} coefficient of the FASTSIM algorithm [37]. The Kalker coefficients c_{ij} used to solve the tangential problem depend on the axis ratio of an elliptical contact path, but in the case of these twin-disc tests the path is rectangular instead of elliptical. The coefficients c_{22}, c_{33} and c_{23} are related to lateral creepage and spin, and therefore should not be fitted.

Although twin-discs machines are widely employed for wear characterisation, these are not as accurate as required for low creepages. The real creepage tested differs slightly from the reference value due to the sensitivity of angular speed measurement. This value is calculated from angular speeds w and radii ratio of both specimens according to

$$\gamma = \frac{w_1 - w_2 \frac{R_2}{R_1}}{0.5\left(w_1 + w_2 \frac{R_2}{R_1}\right)} . \tag{3}$$

Fig. 23 shows that this effect has great importance when very small creepages are considered. For a constant rotational speed of rail specimen of 416 rpm measured with a sensitivity of 0.20 rpm, the error is less than 5 % for longitudinal creepage values higher than 2 %. The light blue dots show the error considered in the analytical calculation of the slipping area. In this manner, the c_{11} coefficient can be fitted for a unique friction coefficient at saturation μ_o. This assumption allows calculating A_{slip} values theoretically, which cannot be obtained by experimental methods.

Fig. 24 shows the analytical adhesion curve used for the calculation of A and the A_{slip}/A ratio for a creepage of 2.53 %. In addition to the fitting of the c_{11} coefficient, the theoretically tested creepages are scattered. This scattering is performed according to the creepage error, with the aim of reducing the value of the coefficient of determination R^2

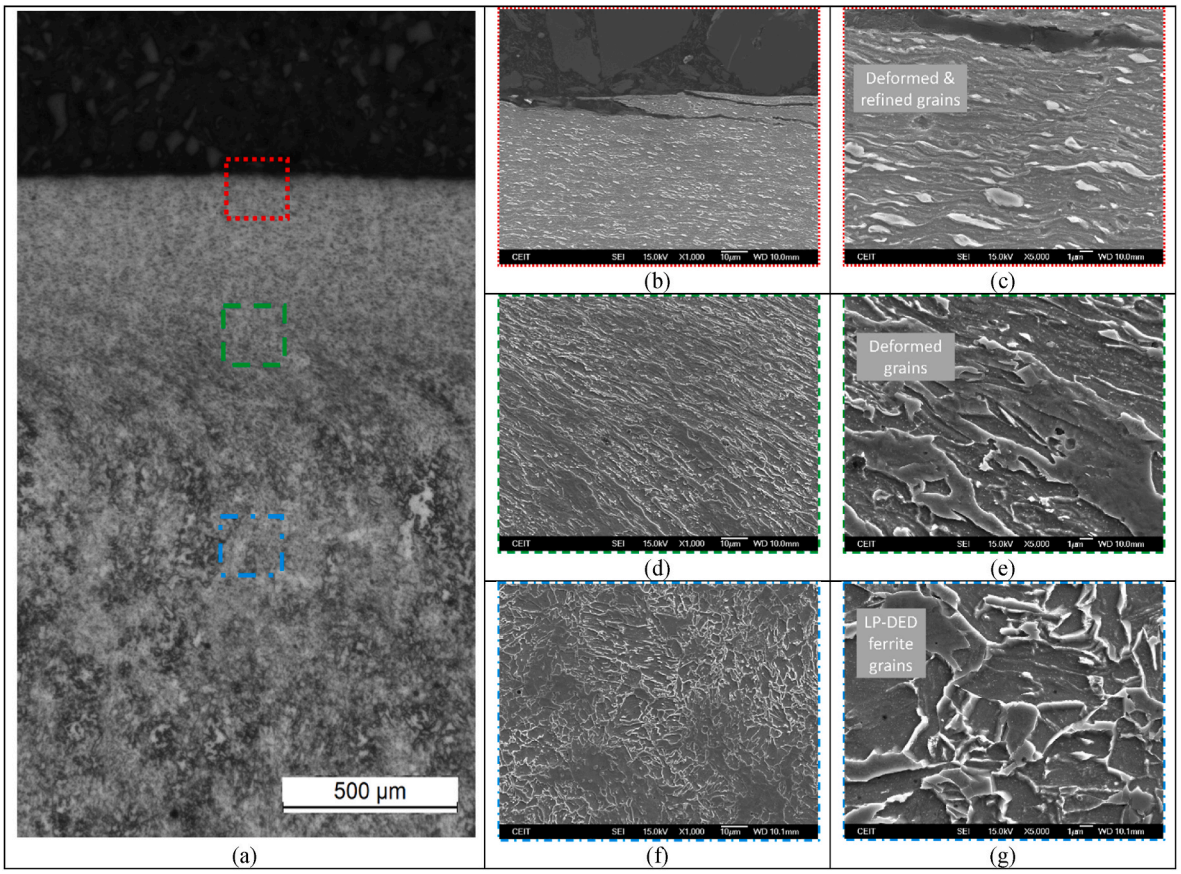

Fig. 16. Optical and SEM micrographs of plastic deformation of 1.5 % creepage of the LP-DED specimen. (a) Optical micrograph. (b and c) SEM micrograph at the surface of the specimen. (d and e) SEM micrograph near the end of the deformed zone of the specimen. (f and g) SEM micrograph at the undeformed microstructure of the specimen.

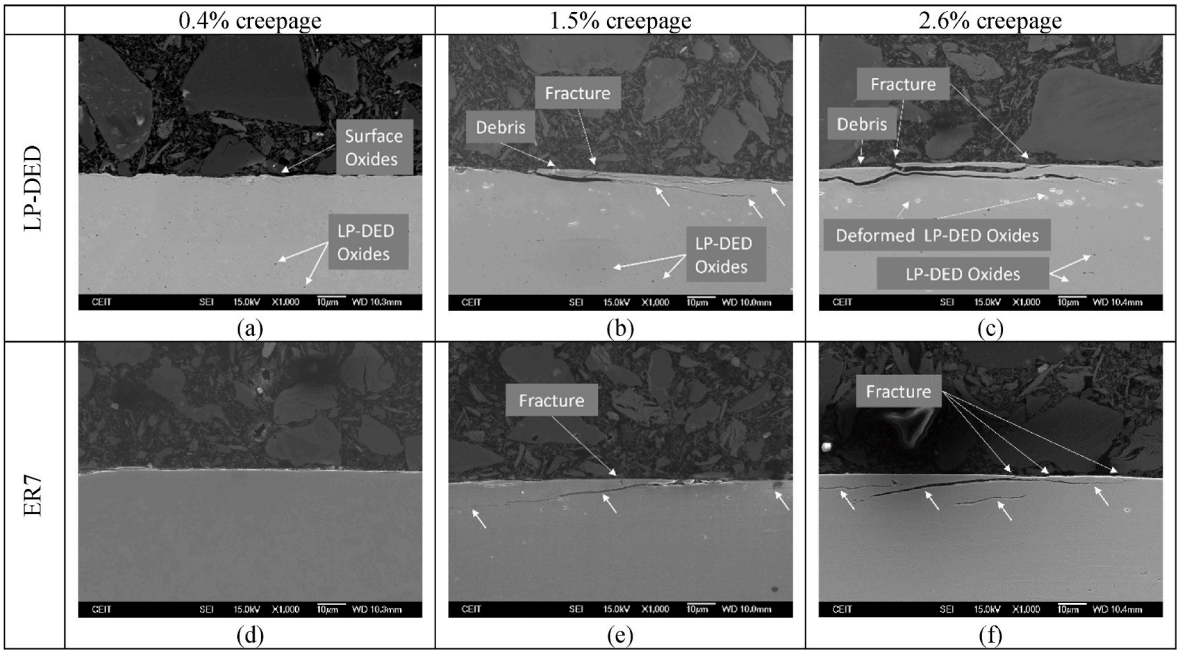

Fig. 17. FEG-SEM Micrographs of cracks in rail and wheel specimens. Cracks pointed with white arrows. 1000× Initial magnification.

for the curve obtained, reaching a value of 0.9989.

Table 3 contains the calculated slipping area A_{slip} for each test carried out considering the scattered creepages. These values, obtained with the FASTSIM algorithm, are not proportional to the creepages, since the creepages tested are not only in the linear zone of the adhesion curve, but also in the non-linear zone. In order to improve the calculated

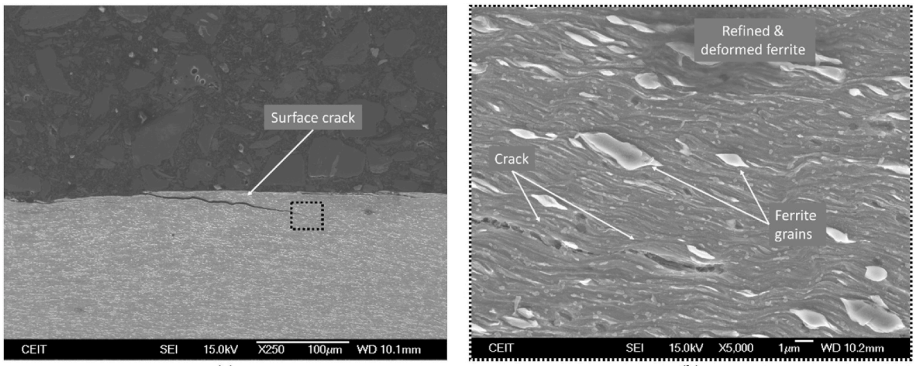

Fig. 18. FEG-SEM Micrographs of the LP-DED specimen tested at 1.5 % creepage. (a) 250x and (b) 5000× of Initial magnification. Crack and crack propagation though ferrite microstructure.

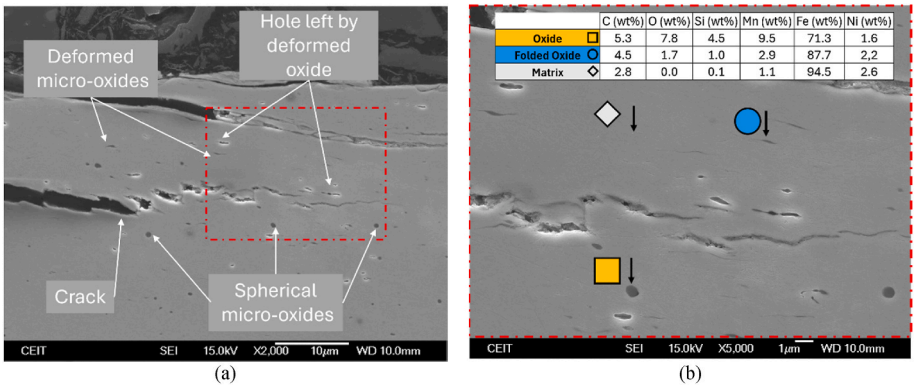

Fig. 19. FEG-SEM Micrographs of the LP-DED specimen tested at 1.5 % creepage. (a) 2000× of Initial magnification, crack propagation jumping through LP-DED oxides. (b) 5000× of Initial magnification, EDS point analysis of oxides and base metal.

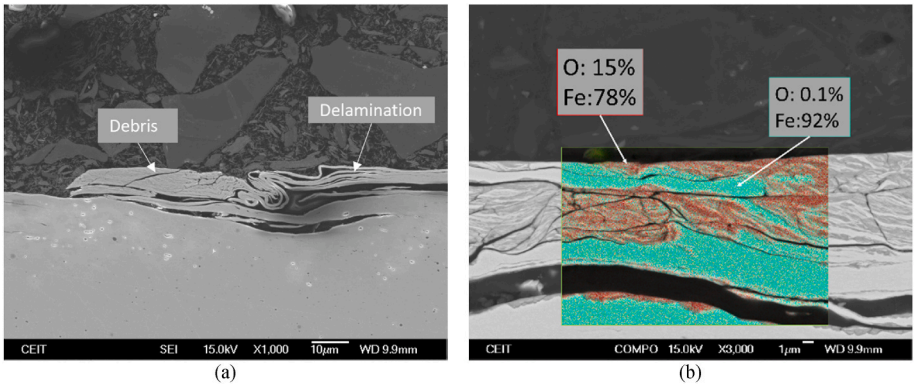

Fig. 20. FEG-SEM Micrographs of debris of the LP-DED specimen tested at 1.5 % creepage. (a) Debris formation due to delamination. (b) EDS analysis of observed debris.

value for A_{slip}/A while neglecting the computational cost, the m x n elements of the mesh employed is of 100 x 100.

Once the A_{slip} for each test is known, the K_{slip} value can be calculated for the *WL* differences obtained in the stages of 20 kilocylces. Fig. 25 shows that K_{slip}, with an average value around 80 μg/(m·mm^2), differs as a function of the creepage value. The obtained values for 1.5 % and 2.0 % creepage are higher and with more deviation than for 0.4 % and 2.6 %. Although raw *WL* values are higher with the creepage value, the influence of calculated A_{slip} makes this phenomenon, which is related to the observed wear mechanisms.

5. Discussion

Once the wear rates at full slip for different creepages are known, for a specific maximum pressure and friction coefficient, a fitted polynomial can be obtained considering the standard deviation. In this way, a K_{slip} value is calculated for any desired creepage value. The results of the test performed in this research using a third-degree polynomial are shown in Fig. 26. An upward trend is observed for K_{slip} values up to 1.5 % of creepage, and a downward trend from this value. Debris and internal oxides could affect the wear rates more intensely at the transition from tribochemical to delaminative wear. As creepage continues increasing

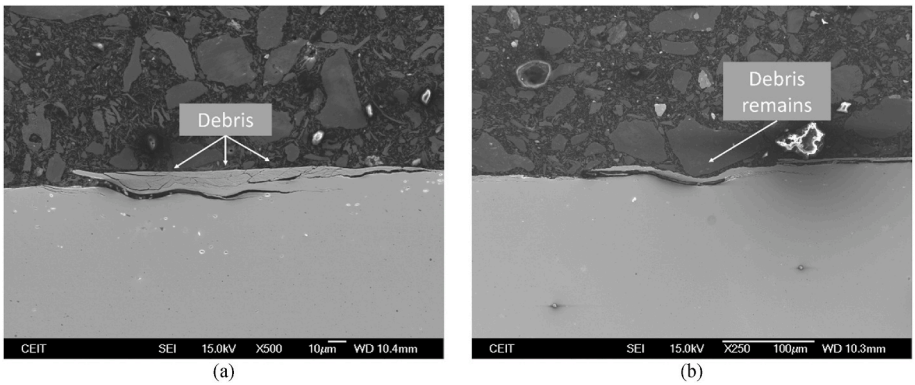

Fig. 21. FEG-SEM Micrographs of the LP-DED specimen tested at 1.5 % creepage. (a) semicontinuous layer of debris and (b) remains of ejected previous debris.

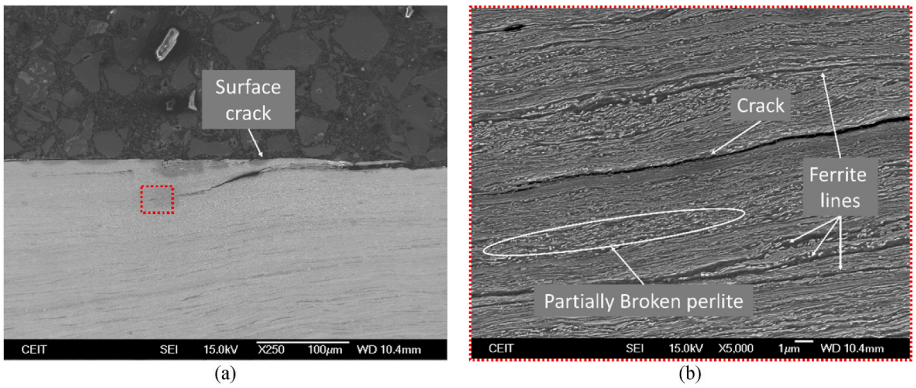

Fig. 22. FEG-SEM Micrographs of ER7 specimen tested at 1.5 % creepage. (a) 250x and (b) 5000× of Initial magnification. Crack and crack propagation though ferrite-perlite microstructure.

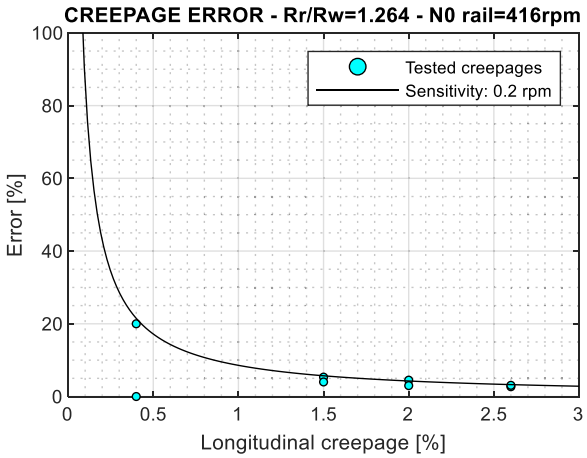

Fig. 23. Creepage error at nominal rail speed of 416 rpm for a sensitivity of 0.2 rpm.

from 1.5 %, its contribution to wear rates decreases and becomes negligible at 2.6 % of creepage.

Wear of a wheel-rail contact patch can be calculated from the full slip wear rates obtained from several twin-disc test conditions. Creepages on wheel-rail contact can be obtained from multibody simulation packages for a certain friction coefficient. As tested adhesion curve obtained with a scaled test bench does not change, the original Kalker coefficients must be employed in the calculation. The normal pressure, the location of contact and the area of the slipping zone can be obtained as well. Therefore, calculating K_{slip} as a function of the creepage from fitted polynomials, knowing the normal pressure and the friction coefficient, is enough to obtain the wear rate at full slip by interpolations. Then, with the area of the slipping zone for wheel-rail contact, the wear prognosis is possible. Nevertheless, future research with measurements of a repaired rail installed on a railway track is required.

6. Conclusions

In this paper, the wear rate of twin-disc specimens manufactured by Laser Powder Directed Energy Deposition using powder grade E11018 material is investigated. The E11018-G, commercially known as OK75.75, is a special material for repairing R260 grade rails and its wear determines the Life Cycle Cost of the asset. In wheel-rail contact, wear rate changes with creepages at contact and this must be considered to calculate accurately the most cost-effective solution for the reparation method.

Experimental tests performed by twin-discs concluded that the weight loss of additively manufactured E11018-G material (LP-DED material) is up to 4 times greater than the conventional R260 when is subjected to different creepages. Regarding the adhesion curve obtained with a scaled test bench, the tangential force that can be obtained for each creepage is equivalent to conventional rail materials.

The surface and metallographic characterisation have shown that low creepeages lead to oxidation phenomena in both specimens. However, higher creepeages lead to delaminative wear, on the LP-DED material and to rolling contact fatigue processes on the ER7 wheel specimens. Debris and internal micro-oxides were found in the LP-DED specimens which influence the obtained wear rates.

The wear rate at full slip can be calculated for a specific creepage value using a fitted polynomial according to the normal pressure and friction coefficient. As the adhesion curve does not change for LP-DED

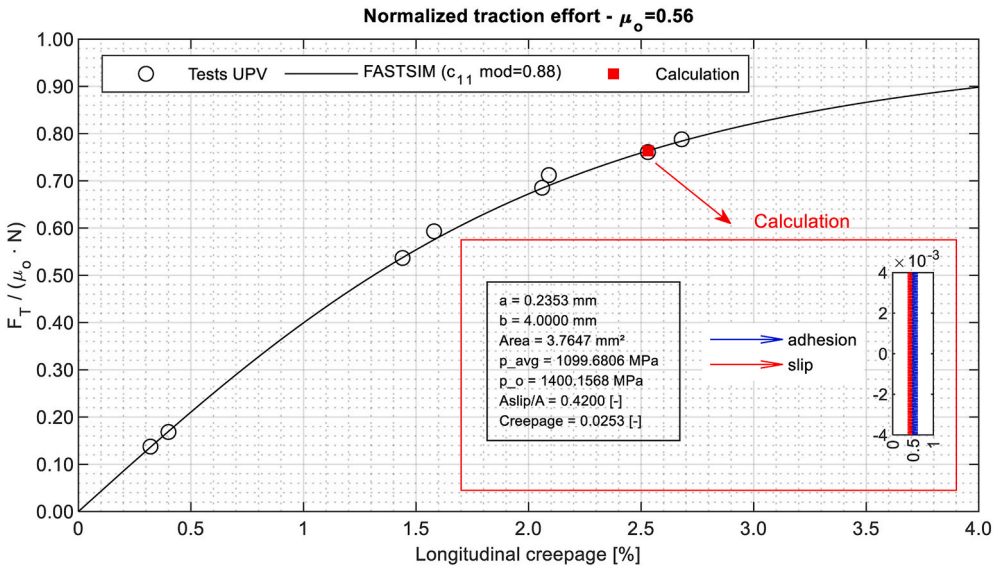

Fig. 24. Analytical adhesion curve from twin-disc tests showing the calculation for 2.53 % of creepage.

Table 3
Slip area for different creepages with $\mu_o = 0.56$ and c_{11} *mod* = 0.88

Creepage	0.32 %	0.40 %	1.58 %	1.44 %	2.09 %	2.06 %	2.53 %	2.68 %
Test	1	2	3	4	5	6	7	8
A (mm^2)	3.76	3.76	3.76	3.57	3.57	3.57	3.76	3.76
A_{slip}/A (−)	0.01	0.02	0.22	0.19	0.33	0.33	0.42	0.45
A_{slip} (mm^2)	0.0376	0.0753	0.8282	0.6782	1.1779	1.1779	1.5812	1.6941

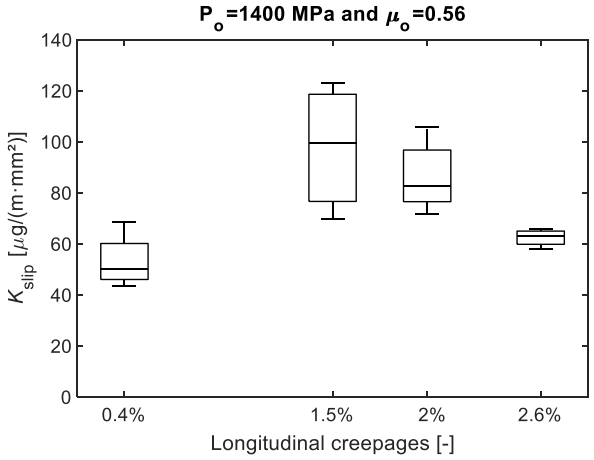

Fig. 25. Wear rates at different creepages for 1400 MPa and a friction coefficient of 0.56.

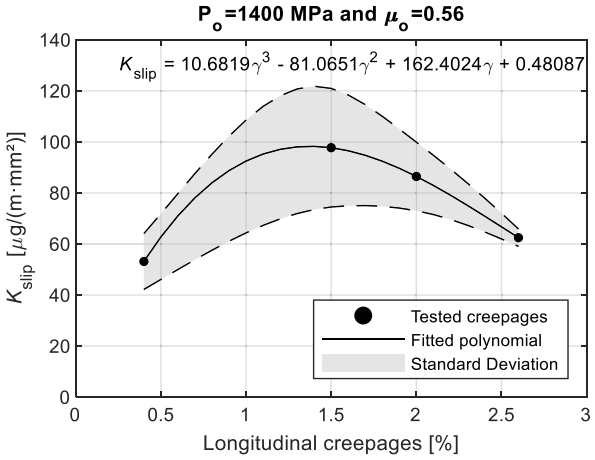

Fig. 26. Fitted polynomial and standard deviation of wear rates at full slip for 1400 MPa and a friction coefficient of 0.56.

material, wheel-rail contact conditions can be obtained directly from multibody simulations without change the Kalker coefficients of the FASTSIM algorithm. Hence, the prognosis of the Life Cycle Cost, assuming a certain standard deviation, can be calculated using parameters such as the creepage value and the slipping contact area for different track sections.

CRediT authorship contribution statement

B. Rodríguez-Arana: Writing – review & editing, Writing – original draft, Visualization, Supervision, Methodology, Investigation, Data curation, Conceptualization. **J. López-López:** Writing – review & editing, Writing – original draft, Visualization, Investigation, Data curation, Conceptualization. **F. Schiopetto:** Writing – review & editing, Investigation. **A. San Emeterio:** Writing – review & editing, Supervision, Investigation. **F. Salas Vicente:** Writing – review & editing, Supervision, Data curation. **I. Pérez-Casero:** Investigation. **A. Veiga:** Writing – review & editing, Writing – original draft, Supervision, Investigation, Conceptualization. **S. Ausejo:** Writing – review & editing, Supervision, Project administration, Funding acquisition.

Declaration of competing interest

The authors declare that they have no known competing financial

interests or personal relationships that could have appeared to influence the work reported in this paper.

Data availability

Data will be made available on request.

Acknowledgements

This work was supported by grant CPP2021-008681 funded by MCIN/AEI/10.13039/501100011033 and by the "European Union NextGenerationEU/PRTR". The authors gratefully acknowledge CAF-MiiRA for providing wheel material.

References

[1] British Standard, Railway applications - track - Restoration of rails by electric arc welding, BS EN 15594) (2009) 1–80.
[2] H.K. Jun, J.W. Seo, I.S. Jeon, S.H. Lee, Y.S. Chang, Fracture and fatigue crack growth analyses on a weld-repaired railway rail, Eng. Fail. Anal. 59 (2016) 478–492, https://doi.org/10.1016/j.engfailanal.2015.11.014.
[3] H. León-Henao, Á.D. Bedoya-Zapata, C. Franco-Rendón, J.F. Santa, J.E.G. Barrada, Avaliação da soldabilidade dos trilhos endurecidos grado r350ht para a reparação de ferrovias com recargos superficiais, Soldagem e Inspecao 25 (2020) 1–15, https://doi.org/10.1590/0104-9224/SI25.37.
[4] K. Tomlinson, D.I. Fletcher, R. Lewis, Evaluation of laser cladding as an in-situ repair method on rail steel, Tribol. Int. 180 (2023), https://doi.org/10.1016/j.triboint.2022.108210.
[5] S.R. Lewis, R. Lewis, D.I. Fletcher, Assessment of laser cladding as an option for repairing/enhancing rails, Wear 330–331 (2015) 581–591, https://doi.org/10.1016/j.wear.2015.02.027.
[6] S.R. Lewis, S. Fretwell-Smith, P.S. Goodwin, L. Smith, R. Lewis, M. Aslam, D. I. Fletcher, K. Murray, R. Lambert, Improving rail wear and RCF performance using laser cladding, Wear 366–367 (2016) 268–278, https://doi.org/10.1016/j.wear.2016.05.011.
[7] P. Lu, S.R. Lewis, S. Fretwell-Smith, D.L. Engelberg, D.I. Fletcher, R. Lewis, Laser cladding of rail; the effects of depositing material on lower rail grades, Wear (2019) 438–439, https://doi.org/10.1016/j.wear.2019.203045.
[8] Y. Zhu, Y. Yang, X. Mu, W. Wang, Z. Yao, H. Yang, Study on wear and RCF performance of repaired damage railway wheels: assessing laser cladding to repair local defects on wheels, Wear 430–431 (2019) 126–136, https://doi.org/10.1016/j.wear.2019.04.028.
[9] H. Ding, X. Mu, Y. Zhu, W. Yang, Q. Xiao, W. Wang, Q. Liu, J. Guo, Z. Zhou, Effect of laser claddings of Fe-based alloy powder with different concentrations of WS2 on the mechanical and tribological properties of railway wheel, Wear (2022) 488–489, https://doi.org/10.1016/j.wear.2021.204174.
[10] L. Meng, B. Zhu, Q. Hu, X. Zeng, D. Wang, Laser-induction hybrid cladding of different coatings on rail surface: microstructure, wear properties and contact fatigue behaviors, Appl. Surf. Sci. 566 (2021), https://doi.org/10.1016/j.apsusc.2021.150678.
[11] C. He, G. Zou, H. Liu, X. Wang, Y. Xu, J. Liu, S. Lo, Rolling–sliding wear and damage behaviors of 304L stainless steel laser cladding on a damaged wheel tread under high ambient temperature conditions, Wear (2024) 546–547, https://doi.org/10.1016/j.wear.2024.205330.
[12] K. Six, A. Meierhofer, G. Müller, P. Dietmaier, Physical processes in wheel-rail contact and its implications on vehicle-track interaction, Veh. Syst. Dyn. 53 (2015) 635–650, https://doi.org/10.1080/00423114.2014.983675.
[13] Y. Hu, L. Zhou, H.H. Ding, G.X. Tan, R. Lewis, Q.Y. Liu, J. Guo, W.J. Wang, Investigation on wear and rolling contact fatigue of wheel-rail materials under various wheel/rail hardness ratio and creepage conditions, Tribol. Int. 143 (2020), https://doi.org/10.1016/j.triboint.2019.106091.
[14] J. Turnia, J. Sinclair, J. Perez, A review of wheel wear and rolling contact fatigue, Proc. Inst. Mech. Eng. F J. Rail Rapid Transit 221 (2007) 271–289, https://doi.org/10.1243/0954409JRRT72.
[15] J.F. Archard, Contact and rubbing of flat surfaces, J. Appl. Phys. 24 (1953) 981–988, https://doi.org/10.1063/1.1721448.
[16] J.F. Archard, W. Hirst, The Wear of Metals under Unlubricated Conditions, 1956.
[17] T. Jendel, Prediction of Wheel Profile Wear-Comparisons with Field Measurements, 2002.
[18] A. Bevan, P. Molyneux-Berry, B. Eickhoff, M. Burstow, Development and validation of a wheel wear and rolling contact fatigue damage model, Wear 307 (2013) 100–111, https://doi.org/10.1016/j.wear.2013.08.004.
[19] I.J., H.R.F. McEwen, Interpretation of Wheel/rail Wear Numbers, vol. 4, TM VDY, 1986.
[20] Anders Ekberg, Elena Kabo, Jonas Ringsberg, Proceedings 6th International Conference on Contact Mechanics and Wear of Rail-Wheel Systems : CM2003 : June 10-13, 2003, vol. I, CHARMEC, Gothenburg, Sweden, 2003.
[21] H. Al-Maliki, A. Meierhofer, G. Trummer, R. Lewis, K. Six, A new approach for modelling mild and severe wear in wheel-rail contacts, Wear 476 (2021), https://doi.org/10.1016/j.wear.2021.203761.
[22] J.J. Kalker, A fast algorithm for the simplified theory of rolling contact, Veh. Syst. Dyn. 11 (1982) 1–13, https://doi.org/10.1080/00423118208968684.
[23] B. Dirks, R. Enblom, M. Berg, Prediction of wheel profile wear and crack growth – comparisons with measurements, Wear 366–367 (2016) 84–94, https://doi.org/10.1016/j.wear.2016.06.026.
[24] I.S. Apezetxea, X. Perez, C. Casanueva, A. Alonso, New methodology for fast prediction of wheel wear evolution, Veh. Syst. Dyn. 55 (2017) 1071–1097, https://doi.org/10.1080/00423114.2017.1299870.
[25] Renfe, NRV 3-0-3-1 Carriles, Reparación de la superficie de rodadura por recargue al arco eléctrico, 1994.
[26] International Union of Railways, UIC Code 712: Rail Defects, UIC, 2002.
[27] D.I. Fletcher, J.H. Beynon, Development of a machine for closely controlled rolling contact fatigue and wear testing, J. Test. Eval. 28 (2000) 267–275, https://doi.org/10.1520/jte12104j.
[28] R. Lewis, E. Magel, W.J. Wang, U. Olofsson, S. Lewis, T. Slatter, A. Beagles, Towards a standard approach for the wear testing of wheel and rail materials, Proc. Inst. Mech. Eng. F J. Rail Rapid Transit 231 (2017) 760–774, https://doi.org/10.1177/0954409717700531.
[29] E. Butini, L. Marini, M. Meacci, E. Meli, A. Rindi, X.J. Zhao, W.J. Wang, An innovative model for the prediction of wheel - rail wear and rolling contact fatigue, Wear 436–437 (2019) 203025, https://doi.org/10.1016/j.wear.2019.203025.
[30] F. Braghin, R. Lewis, R.S. Dwyer-Joyce, S. Bruni, A mathematical model to predict railway wheel profile evolution due to wear, Wear 261 (2006) 1253–1264, https://doi.org/10.1016/j.wear.2006.03.025.
[31] C. Hardwick, R. Lewis, D.T. Eadie, Wheel and rail wear-Understanding the effects of water and grease, Wear 314 (2014) 198–204, https://doi.org/10.1016/j.wear.2013.11.020.
[32] S.R. Lewis, S. Fretwell-Smith, P.S. Goodwin, L. Smith, R. Lewis, M. Aslam, D. I. Fletcher, K. Murray, R. Lambert, Improving rail wear and RCF performance using laser cladding, Wear 366–367 (2016) 268–278, https://doi.org/10.1016/j.wear.2016.05.011.
[33] L. Deters, M. Proksch, Friction and wear testing of rail and wheel material, in: Wear, 2005, pp. 981–991, https://doi.org/10.1016/j.wear.2004.03.045.
[34] Y. Hu, W.J. Wang, M. Watson, K. Six, H. Al-Maliki, A. Meierhofer, R. Lewis, Wear of driving versus driven discs in a twin disc rolling-sliding test, Wear (2023) 512–513, https://doi.org/10.1016/j.wear.2022.204528.
[35] A. Alonso, A. Guiral, L. Baeza, S. Iwnicki, Wheel-rail contact: experimental study of the creep forces-creepage relationships, in: Vehicle System Dynamics, 2014, pp. 469–487, https://doi.org/10.1080/00423114.2014.907923.
[36] J.J. Kalker, Simplified theory of rolling contact, Delft Prog. Rep. (1973).
[37] J.J. Kalker, A fast algorithm for the simplified theory of rolling contact, Veh. Syst. Dyn. (1982) 37–41, https://doi.org/10.1080/00423118208968684.
[38] R. Lewis, R.S. Dwyer-Joyce, U. Olofsson, J. Pombo, J. Ambrósio, M. Pereira, C. Ariaudo, N. Kuka, Mapping railway wheel material wear mechanisms and transitions, in: Proc Inst Mech Eng F J Rail Rapid Transit, 2010, pp. 125–137, https://doi.org/10.1243/09544097JRRT328.
[39] H.H. Ding, Z.K. Fu, W.J. Wang, J. Guo, Q.Y. Liu, M.H. Zhu, Investigation on the effect of rotational speed on rolling wear and damage behaviors of wheel/rail materials, Wear 330–331 (2015) 563–570, https://doi.org/10.1016/j.wear.2014.12.043.
[40] H.H. Ding, C.G. He, L. Ma, J. Guo, Q.Y. Liu, W.J. Wang, Wear mapping and transitions in wheel and rail materials under different contact pressure and sliding velocity conditions, Wear 352–353 (2016) 1–8, https://doi.org/10.1016/j.wear.2016.01.017.
[41] B. Rodríguez-Arana, A. San Emeterio, M. Panera, A. Montes, D. Álvarez, Investigation of a relationship between twin-disc wear rates and the slipping contact area on R260 grade rail, Tribol. Int. 168 (2022), https://doi.org/10.1016/j.triboint.2022.107456.
[42] B. Eghbali, Study on the ferrite grain refinement during intercritical deformation of a microalloyed steel, Mater. Sci. Eng., A 527 (2010) 3407–3410, https://doi.org/10.1016/j.msea.2010.01.075.
[43] J.E. King, P.J. Cotterill, Role of Oxides in Fatigue Crack Propagation, 1990.